DR THORSTEN J. NAGEL (Orcid ID : 0000-0001-6158-4052)

Article type : Paper

Received date: 22-Feb-2018

Revised version received date: 17-Jun-2018

Accepted date: 01-Jul-2018

Correspondence details:

Dr Thorsten J. Nagel

Tel: +4587156298

E-mail: thorsten.nagel@geo.au.dk

Garnet-controlled very low velocities in the lower mantle transition zone at sites of mantle upwelling

Thorsten J. Nagel, Department of Geoscience, Aarhus University, Aarhus, Denmark

Erik Duesterhoeft, Department of Geoscience, Christian-Albrechts University, Kiel, Germany

Christian Schiffer, Department of Earth Sciences, Durham University, Durham, UK

This article has been accepted for publication and undergone full peer review but has not been through the copyediting, typesetting, pagination and proofreading process, which may lead to differences between this version and the Version of Record. Please cite this article as doi: 10.1111/ter.12348

Key words:

mantle plume, mantle transition zone, receiver functions, seismic velocity modelling, 660 discontinuity

Abstract

Deep mantle plumes and associated increased geotherms are expected to cause an upward deflection of the lower–upper mantle boundary and an overall thinning of the mantle transition zone between about 410 and 660 kilometres depth. We use subsequent forward modelling of mineral assemblages, seismic velocities and receiver functions to explain the common paucity of such observations in receiver function data. In the lower mantle transition zone, large horizontal differences in seismic velocities may result from temperature-dependent assemblage variations. At this depth, primitive mantle compositions are dominated by majoritic garnet at high temperatures. Associated seismic velocities are expected to be much lower than for ringwoodite-rich assemblages at undisturbed thermal conditions. Neglecting this ultra-low-velocity zone at upwelling sites can cause a miscalculation of the lower–upper mantle boundary on the order of 20 kilometres.

1. Introduction

Hot-spot magmatism occurs at sites of convective mantle upwelling. With the timescale of upward motion short compared to the timescale of conductive thermal equilibration, mantle material would decompress adiabatically and cross its solidus. Most studies propose a lower-mantle source for the rising material (Morgan, 1972;

De Paolo and Manga, 2003). Accordingly, the material stream would cross the mantle transition zone (MTZ), the lower part of the upper mantle between about 410 and 660 kilometres depth. The MTZ is bounded by two phase transitions (the 410 and the 660 transitions, respectively), which correspond to considerable density and seismic-velocity discontinuities and thus produce large amplitude seismic signals in receiver function (RF) data (e.g. Stammler *et al.*, 1992; Vinnik *et al.*, 1996; Lawrence and Shearer, 2006; Andrews and Deuss, 2008). The bottom of the MTZ (660 discontinuity) is the boundary between the upper and lower mantle and corresponds to the downward replacement of ringwoodite with periclase plus Mg–Si-perovskite, also called bridgmanite. The top of the MTZ (410 discontinuity) is defined by the downward replacement of olivine with wadsleyite. The 660 transition has a negative Clapeyron slope while the 410 transition has a positive slope with similar absolute values of 2–3 MPa/K (Hirose, 2002; Gasparik, 2003; Deuss *et al.*, 2013, Figure 1). The slope of the 660 transition is actually controversial with some estimates as high as -1 MPa/K. Most experiments, first-principle calculations and fundamental seismic studies (e.g. Hirose, 2002; Yu et al., 2007; Hernández et al., 2015; Tauzin and Ricard, 2014), however, point to values lower than -2 MPa/K (Cottaar and Deuss, 2015). Because of the opposite slopes of the bounding reactions, the MTZ should become thinner with increasing geothermal gradients (Bina and Helffrich, 1994). Yet, observations at hotspot sites have been ambiguous. While the 410 discontinuity typically does show the expected downward excursion, the behaviour of the 660 discontinuity is less consistent. In Iceland, Jenkins et al. (2016) found the bottom of the MTZ displaced downward and attributed this to a garnet-related positive Clapeyron slope at high temperatures. Recent RF data from Hawaii show overall moderate topography of the 660 discontinuity with upward and downward displacements (Agius et al., 2017; see also Cao et al., 2011). Similar observations exist from the East African Rift (e.g. Huerta et al. 2009; Cornwell, 2011), the Western US (Gao and Liu, 2014), and South China (Huang et al., 2015). We present progressive forward modelling of mineral assemblages (Figure 1, 2), seismic velocities (Figure 3) and 1D RFs (Figure 4, 5) along various adiabats. Assemblage evolutions are similar for different adiabats except for the lower MTZ where garnet-rich assemblages may cause a pronounced low-velocity anomaly for hot geotherms. This low-velocity zone would account for larger-than-expected delay times at hot spot sites, which may lead to artificial deepening of the 660 discontinuity in seismic observations, if unaccounted for in time–depth conversions.

2. Modelling phase relations, seismic velocities and receiver functions

The emergence of thermodynamic databases allowing for quantitative modelling of assemblages at mantle conditions (Stixrude and Lithgow-Bertelloni, 2011; Holland *et al.*, 2013) has provided a powerful tool to study mantle processes and their seismic footprints (e.g. Xu et al., 2008; Stixrude and Lithgow-Bertelloni, 2012; Cammarano, 2013; Shorttle *et al.*, 2014). We use Theriak/Domino software (De Capitani and Petrakakis, 2010) and the database from Holland et al. (2013) to explore phase relations in primitive mantle (Figure 1). The composition employed here is from Lyubetskaya and Korenaga (2007). Other common propositions yield almost identical phase relations (supporting information, figure S1). Along with the thermodynamic calculations come density-, entropy- and Gibbs-free-energy, which are further utilized in the subsequent modelling. Adiabats shown in Figure 1 are calculated from the entropy of the predicted stable mineral assemblages and used to approximate primitive mantle geotherms down to 800 kilometres depth (30 GPa) for potential temperatures of 1350 °C, 1450 °C, 1550 °C and 1650 °C (at 3 GPa), respectively. Synthetic profiles of seismic velocities (Figure 2, 3b) are derived from assemblages, using the Theriak_D add-on (Duesterhoeft and de Capitani, 2013). We used a novel heuristic technique for calculating the shear modulus needed for computation of seismic velocities as a function of temperature, pressure and composition (see supporting information for a detailed description).

The RF method is a common tool to image seismic discontinuities, traditionally in the crust and upper mantle, by deconvolving waveforms of incident teleseismic P-waves that are converted to S-waves (e.g. Langston, 1979; Vinnik, 1977; Ammon, 1991; Kind *et al.*, 1995). The P-to-S conversions are visualized as pulses at the delay time of the converted S-wave after the P-wave. This delay time is dependent on the depth of the discontinuity, the overlying S and P wave velocity structure and the ray parameter (Zhu and Kanamori, 2000). A RF with known parameters of an incident earthquake may thus be back-migrated from delay time to the true conversion point, if the overlying velocities are known, while usage of a wrong velocity model may lead to errors in depth (Tauzin and Ricard, 2014). We produce synthetic 1D RFs of the thermodynamically estimated velocity–density models, which are initially translated from pressure to depth. These synthetic MTZ images are idealized, perfectly depth-migrated and noise-free. Real data would be obscured by noise, scattering and imaging artefacts; however, the target of this study is to identify first-order characteristics of the time–depth migration of major discontinuities and the effect of velocity models. These effects will show robustly in real data. The pressure–depth conversion in our modelling assumes a lithostatic depth defined by densityintegration along the 1350 °C adiabat and extended by a standard continental lithosphere at the top (35 km thick crust with a density of 2800 kg/m^3 and 100 km thick lithospheric mantle with a density of 3300 kg/m^3). Hence, we assume pressure equilibrium between upwelling and ambient mantle. Synthetic RFs are calculated using the velocity–density–depth profiles (supporting information, figure S2) and a 1D wavefield code to compute the surface response to an incoming plane wave (Kennett, 1983) and subsequent waterlevel-deconvolution with a Gaussian factor of 2 (e.g. Clayton and Wiggins, 1976; Langston 1979) (supporting information, figure S3 shows the effect of different Gaussian filters). As for real RFs, the synthetics are given in delay time (Fig. 4a). The lithospheric layers are removed and constant lithospheric velocities (Vs=4.5 km/s, Vp=8.1 km/s) are assumed in the upper 135 km to obtain MTZ signals undisturbed by multiple conversions (supporting information, figure S4 shows the negligible effect of multiples). Thereafter, the RFs are converted to depth (Figure 4b).

3. Results

Figure 1 shows the classic phase transitions bordering the MTZ, i.e. the 410 and the 660 discontinuities. Narrowing of the MTZ with increasing temperature is predicted to occur up to 1800 ºC, where the slope of the 660 transition becomes positive. This slope change reflects the changeover from the assemblage ringwoodite/wadsleyite + garnet + Ca–Si-perovskite to majorite-rich garnet + periclase, which takes place towards high temperatures in the MTZ. The associated reactions are continuous and may start below 1650 ºC at 20 GPa. Figure 2 displays predicted assemblage evolutions and seismic velocities following adiabats in figure 1. The above-described reaction represents by far the most significant difference in assemblage evolution between normal and high-temperature scenarios. At pressures below 16 GPa and above 24 GPa, assemblages evolve similarly. In the lower MTZ, however, majoritic garnet + periclase progressively replaces Mg_2SiO_4 phases towards higher temperatures. This leads to the complete disappearance of ringwoodite at 20 GPa along the 1650 ºC adiabat. The horizontal mineralogical variation in the lower MTZ is associated with a significant reduction in velocity (Figure 2–4). While below and above the MTZ, temperature-dependent velocity differences would be in the order of the typical tomographic signal, i.e. 1–1.5%, velocities in the lower MTZ display a pronounced fanning with differences up to about 7% for S-waves and 5% for P-waves (Figure 3b). Figure 4 shows synthetic RFs. The 410 and 660 discontinuities produce the expected large amplitude positive conversion signals. The 410 discontinuity shows a clear deepening with higher temperatures. The 660 discontinuity displays less pronounced depth differences although the negative pressure–temperature slope has similar amplitude. Because of higher densities in the lowermost MTZ compared to the top of the MTZ, the depth–temperature slope of the 660 transition is diminished. Also, the assemblage and property change across the 660 transition is distributed over a depth range of 30 km resulting in a more diffuse signal compared to the 410 discontinuity, which spreads over a depth interval of only 10 km (Figure 3b). The 1650 °C adiabat cuts the 660 transition above 1800 °C, where the Clapeyron slope has turned positive and the RF signal starts to deepen again (Figure 1, 4b). The wadsleyite–ringwoodite transition (often called the 520 transition) produces a small positive conversion along the 1350 °C adiabat. At elevated temperatures, the phase-change-related decrease of velocities with depth results in a low-amplitude negative conversion signal at 530–580 kilometres depth.

This signal, both as a positive and negative 520 discontinuity, might be challenging to resolve in real data; the impact of the low-velocity layer on delay times, however, is robust and momentous.

The MTZ is predicted to show only minor shortening of the delay time width with increasing temperature (Figure 4a). The depth difference of the 660 discontinuity between the 1350 and the 1550 adiabat is outweighed by the velocity difference in the lower MTZ, causing a larger delay time for warmer adiabats (Figure 4a). Although the 660 discontinuity is 8 kilometres shallower along the 1650 ºC than along the 1350 ºC adiabat (Figure 4b), its delay time is 1.8 seconds longer. Figure 5 illustrates the effects of the low-velocity zone in the lower MTZ on the inferred depth of the 660 discontinuity using different velocity models for time–depth conversion. Using the velocity model of the 1350 °C adiabat to convert the RFs of the 1650 °C adiabat (Figure 4a) leads to a 660 discontinuity estimation 26 km too deep. Even if a general temperature-related velocity reduction of 1.5% - the typical magnitude inferred in tomographic models - is assumed and the model is corrected for the altered location of the 410 discontinuity (Figure 5b), the 660 discontinuity is still placed 17 km too deep.

4. Discussion

Some recent studies have used compositional variations to explain the seismic signature of different tectonic environments (e.g. Adam *et al.*, 2017; Maguire *et al.*, 2017). A rising plume, however, cannot carry more than 10% of dense MORB and should mainly consist of primitive mantle material (Brown and Lesher, 2014; Shorttle et al., 2014). Accordingly, the seismic signature of a plume would essentially be that of primitive mantle and we propose that the riddle of the little affected MTZ thickness below hot spots can be solved following that assumption. Our explanation rests on two keystones: the discussed temperature-dependent phase change in the lower MTZ and the comparatively low seismic velocities of Mg-rich, majoritic garnet. Both these essentials have been robustly confirmed in experimental and theoretical studies. The decay of ringwoodite to form a majorite component and periclase is well-known in experimental petrology. In a pyrolite composition, it takes place between about 1650 °C and 1800 °C at pressures of 20–23 GPa (e.g. Hirose, 2002; Gasparik, 2003; Ishii *et al.*, 2011; Deuss *et al.*, 2013). More enriched compositions show the reaction even at slightly lower temperatures (supporting material, Figure S1 and S5). The other keystone, a high Poisson's ratio and associated low seismic velocities of majoritic garnet compared to ringwoodite, is also well established in experimental work and theoretical modelling (e.g. Sinogeikin *et al.*, 1997; Sinogeikin and Bass, 2002; Irifune *et al.*, 2002; Liu *et al.*, 2016; Chantel *et al.*, 2016). Using other approaches, i.e. the database from Stixrude and Lithgow-Bertelloni (2011) together with Perplex software (Connolly, 2005), likewise yields the phase-change-related and characteristic fanning of velocities in the lower MTZ (supporting material, figure S6-S9, see also Xu et al. 2008).

Our velocity modelling predicts an S-wave anomaly of up to 7% for warm adiabats (1650°C). Due to limited resolution and ray coverage, such a velocity anomaly might not be seen as pronounced and confined in tomographic images as a forward model would suggest. In the recent paper of Maguire et al. (2017), the forward computed velocity models of various plume scenarios do suggest low velocities in the lower MTZ; however, the inverse tomographic image fails to recover the vertical extent of these layers. Velocity models based on tomographic results alone might thus be insufficient.

The 520 discontinuity on top of the lower MTZ is an elusive boundary which may display negative or positive signals, double peaks, or may even be absent (e.g. Chevrot et al. 1999, Andrews and Deuss, 2008; Deuss *et al.*, 2013; Huang et al. 2015). A low-velocity anomaly in the lower MTZ at mantle-upwelling sites has been proposed in several studies based on negative conversions in RF data. Shen and Blum (2003) observed a negative conversion between 570 and 600 kilometres depth in South Africa and subsequently at several other sites (Shen *et al.*, 2014). Vinnik *et al.* (2005) found a negative conversion at a depth of about 500 kilometres around Iceland and 4 other hot spot locations (Vinnik *et al.*, 2006). These observations were attributed to MORB material possibly accumulated in the lower MTZ (Shen et al., 2014) or dehydration melting during heating of water-saturated wadsleyite in the lower MTZ (Vinnik *et al.*, 2006). However, MORB would be abundant in Fe-rich garnet with properties very different from majorite-rich garnet in primitive mantle. In modelling, it consistently yields higher velocities than the surrounding mantle in the MTZ (e.g. Shorttle *et al.*, 2014). Also, plumes from the lower mantle are expected to be relatively dry. An explanation by means of elevated temperatures and Mg-rich majoritic garnet in primitive mantle offers a simple and elegant alternative explanation for negative conversions observed in the MTZ.

Acknowledgements

This study was supported by a starting grant of *Aarhus Universitets Forskningsfond* to Thorsten Nagel and a postdoctoral fellowship of the *Carlsberg Foundation* to Christian Schiffer.

Figure Captions

Figure 1. Equilibrium phase diagram for a primitive mantle composition [Lyubetskaya and Korenaga, 2007]. Molar abundances of elements in simplified bulk composition used for the calculation are: Si, 38.34; Al, 3.510; Fe, 5.64; Mg, 49.80; Ca, 2.530; Na, 0.49; O, 139.200. Red lines and shaded area highlight the mantle transition zone. Dashed lines are isentropes representing adiabatic geotherms defined by potential temperatures of 1350 °C (blue), 1450 °C (green), 1550 °C (red), and 1650 °C (pink) at 3 GPa, respectively. Mineral abbreviations are: cfe, Ca-ferrite; cpv, Ca–Si-perovskite; cpx, clinopyroxene; grt, garnet; hpx, high-pressure polymorph of cpx; mpv, Mg–Si-perovskite (bridgemanite); nal, NAL phase (Mookerhejee et al., 2012); ol, olivine; opx, orthopyroxene; per, periclase; rw, ringwoodite; wd, wadsleyite. Assemblages: 1, wd + grt + cpx; 2, wd + grt + cpx + hpx; 3, wd + rw + grt; 4, wd + rw + grt + per; 5, rw + grt + per; 6, rw + grt + per + cpv; 7, rw + grt + cpv + nal; 8, rw + grt + cpv + nal + per; 9, mpv + grt + cpv + nal + per; 10, grt + per + cpv. See text for more calculation details.

Figure 2. Assemblages along 4 adiabats displayed in figure 1. Figure 2a to 2d correspond to 1350-, 1450-, 1550-, and 1650- adiabats, respectively. Dashed and solid black lines show velocities of P- and S-waves, respectively. Mineral abbreviations are the same as in figure 1.

Figure 3. Calculated densities (a) and velocities of P- and S-waves (b) along the four adiabats in figure 1. See supporting material for calculation details.

Figure 4. Modelled receiver function (RF) signals along the 1350- (blue), 1450- (green), 1550- (red) and 1650- (pink) adiabats, respectively (fig. 1). 4a: RFs vs. delay time calculated from the depth-converted models from figure 3b (supporting material, figure S2). 4b: RFs vs. depth back-migrated from delay times in figure 4a. Insets highlight RF signals bounding the mantle transition zone. The transition zone thicknesses for different adiabats are 247 km (1350, blue), 237 km (1450, green), 228 km (1550, red) and 224 km (1650, pink). The delay time differences between the 410 and 660 discontinuities are 22.7 sec (1350, blue), 21.9 sec (1450, green), 21.45 sec (1550, red) and 21.7 sec (1650, pink).

Figure 5. Depth-converted RF signals for the 1650- adiabat from figure 4a (5a) using 3 different velocity–depth models for depth conversion (5b). Pink: velocity model of the 1650 adiabat placing RF signals at the proper depth (true model). Blue: Velocity model of the 1350 adiabat, yielding predictions too deep because of the higher velocities. Green: Velocity model of the 1350 adiabat assuming a general velocity

reduction of 1.5% and a corrected depth of the 410 transition, still yielding a prediction around 17 kilometres too deep for the 660 discontinuity as the low velocity zone in the lower mantle transition zone is not accounted for. The transition zone thicknesses for the three models are 224 km (pink), 231 km (green) and 241 km (blue).

References

Adam, C., Caddick, M.J. and King, S.D., 2017. Pyroxenite causes fat plumes and stagnant slabs. *Geophys. Res. Lett., 44, 4730–4737.*

Agius, M.R., Rychert, C.A., Harmon, N. and Laske, G., 2017. Mapping the mantle transition zone beneath Hawaii from Ps receiver functions: Evidence for a hot plume and cold mantle downwellings. *Earth Planet. Sci. Lett., 474, 226-236.*

Ammon, C. J., 1991. The isolation of receiver effects from teleseismic P waveforms. *Bull. seism. Soc. Am., 81, 2504–2510.*

Andrews, J., and Deuss, A., 2008. Detailed nature of the 660km region of the mantle from global receiver function data*. J. Geophys. Res., Solid Earth, 113, B06304, doi: 10.1029/2007JB005111.*

Bina, C. R., and Helffrich, G., 1994. Phase transition Clapeyron slopes and transition zone seismic discontinuity topography. *J. Geophys. Res., 99(B8), 15853–15860, doi: 10.1029/94JB00462.*

Brown, E. L., and Lesher, C.E., 2015. North Atlantic magmatism controlled by temperature, mantle composition and buoyancy. *Nature Geosci., 7, 820-824.*

Cammarano, F., 2013. A short note on the pressure-depth conversion for geophysical interpretation. *Geophys. Res. Lett.*, 40, 4834-4838.

Cao, Q., van der Hilst, R.D., de Hoop, M.V., Shim, S.-H., 2011. Seismic Imaging of Transition Zone Discontinuities Suggests Hot Mantle West of Hawaii, *Science*, 332, 1068-1071.

Chevrot, S., Vinnik, L., Montagner, J.-P., 1999. Global-scale analysis of the mantle Pds phases, *J. Geophys. Res.*,104, 20203-20219.

Clayton, R.W., and Wiggins, R.A., 1976. Source shape estimation and deconvolution of teleseismic bodywaves*, Geophys. J. R. Astron. Soc.*, 47, 151–177.

Connolly, J.A.D., 2005. Computation of phase equilibria by linear programming: A tool for geodynamic modelling and its application to subduction zone decarbonation. *Earth Planet. Sci. Lett., 236, 524-541.*

Cornwell, D.G., Hetényi, G. and Blanchard, T.D., 2011. Mantle transition zone variations beneath the Ethiopian Rift and Afar: Chemical heterogeneity within a hot mantle? *Geophys. Res. Lett., 38, L16308, doi:10.1029/2011GL047575.*

Cottaar, S., and Deuss, A., 2016. Large-scale mantle discontinuity topography beneath Europe: Signature of akimotoite in subducting slabs. *J. Geophys. Res. Solid Earth*, 121, 279–292.

De Capitani, C. and Petrakakis, K., 2010. The computation of equilibrium assemblage diagrams with Theriak/Domino software. *Am. Mineral., 95, 1006–1016.*

De Paolo, D.J., and Manga, M., 2003. Deep Oroigin of Hotspots - the Mantle Plume Model. *Science, 300, 920-921.*

Deuss, A., Andrews, J. and Day, E., 2013. Seismic observations of mantle discontinuities and their mineralogical and dynamical interpretation. In: *Physics and Chemistry of the Deep Earth* (S.-I. Karato, ed.), 295–323, John Wiley & Sons, Ltd, Chichester, UK.

Duesterhoeft, E., and de Capitani, C., 2013. Theriak_D: An add-on to implement equilibrium computations in geodynamic models. *Geochem. Geophys. Geosyst.,* 14, 4962–4967, doi: 10.1002/ggge.20286.

Gao, S.S. and Liu, K.H., 2014. Mantle transition zone discontinuities beneath the contiguous United States. *J. Geophys. Res.,* 119, 6452–6468, doi: 10.1002/2014JB011253.

Gasparik, T.I., 2003. Phase Diagrams for Geoscientists. An Atlas of the Earth's Interior, Springer, Berlin, 1-462.

Hernández, E., Brodholt, J. and Alfè, D., 2015. Structural, vibrational and thermodynamic properties of Mg2SiO4 and MgSiO3 minerals from first-principles simulations. *Phys. Earth Planet. Inter.*, 240, 1–24.

Hirose, K., 2002. Phase transitions in pyrolitic mantle around 670-km depth: Implications for upwelling of plumes from the lower mantle. *J. Geophys. Res.,* 107(B4), doi: 10.1029/2001JB000597.

Holland, T.J.B., Hudson, N.F.C., Powell, R. and Harte, B., 2013. New Thermodynamic Models and Calculated Phase Equilibria in NCFMAS for Basic and Ultrabasic Compositions through theTransition Zone into the Uppermost Lower Mantle. *J. Petrol.*, 54, 1901-1920.

Huang, H., Tosi, N., Chang, S.-J., Xia, S. and Qiu, X., 2015. Receiver function imaging of the mantle transition zone beneath the South China Block. *Geochem. Geophys. Geosyst.,* 16, 3666–3678, doi: 10.1002/2015GC005978.

Huerta, A., Nyblade, A.A. and Reusch, A., 2009. Mantle transition zone beneath Kenya and Tanzania: More evidence for deep-seated thermal upwelling in the mantle, *Geophys. J. Int.*, 177, 1249–1255.

Irifune, T., Higo, Y., Inoue, T., Kono, Y., Ohfuji, H. and Funakoshi, K., 2008. Sound velocities of majorite garnet and the composition of the mantle transition region. *Nature*, 451, 814–817.

Ishii, T., Kojitani, H. and Akaogi, M., 2001. Post-spinel transitions in pyrolite and Mg2SiO4 and akimotoite–perovskite transition in MgSiO3: Precise comparison by high-pressure high-temperature experiments with multi-sample cell technique. *Earth Planet. Sci. Lett.*, 309, 185-197.

Jenkins, J., Cottaar, S., White, R.S. and Deuss, A., 2016. Depressed mantle discontinuities beneath Iceland: Evidence of agarnet controlled 660 km discontinuity? *Earth Planet. Sci. Lett.*, 433, 159-168.

Kennet, B.L.N., 1983. Seismic wave propagation in stratified media by B.L.N. Kennett. *Cambridge University Press.*

Kind, R., Kosarev, G.L. and Petersen, N.V., 1995. Receiver functions at the stations of the German Regional Seismic Network (GRSN). *Geophys. J. Int.,* 121, 191–202.

Langston, C.A., 1979. Structure under Mount Rainier, Washington, inferred from teleseismic body waves, *J. Geophys. Res*. 84(B9), 4749–4762, doi: 10.1029/JB084iB09p04749.

Lawrence, J.F., and Shearer, P.M., 2006. A global study of transition zone thickness using receiver functions. *J. Geophys. Res.,* 111, B06307, doi: 10.1029/2005JB003973.

Liu, X., Xiong, Z., Chang, L., He, Q., Wang, F., Shieh, S.R., Wu, C., Li, B. and Zhang, L., 2016. Anhydrous ringwoodites in the mantle transition zone: Their bulk modulus, solid solution behaviour, compositional variation, and sound velocity feature. *Solid Earth Sciences*, 1, 28-47.

Lyubetskaya, T., and Korenaga, J., 2007. Chemical composition of Earth's primitive mantle and its variance: 1. Method and results. *J. Geophys. Res.,* 112, B03211, doi: 10.1029/2005JB004223.

Maguire, R., Ritsema, J. and Goes, S., 2017. Signals of 660 km topography and harzburgite enrichment in seismic images of whole-mantle upwellings. *Geophys. Res. Lett*., 44, 3600–3607.

Mookherjee, M., Karki, B.B., Stixrude, L. and Lithgow-Bertelloni, C., 2012. Energetics, equation of state, and elasticity of NAL phase: Potential host for alkali and aluminum in the lower mantle. *Geophys. Res. Lett.,* 39, L19306, doi: 10.1029/2012GL053682.

Morgan, W. J., 1972. Plate Motions and Deep Mantle Convection. In: *Studies in Earth and Space Sciences* (R. Shagam, R.B. Hargraves, W.J. Morgan, F.B. Van Houten, C.A. Burk, H.D. Holland, L.C. Hollister eds.), GSA Memoirs 132, 7-22.

Shen, X., Yuan, X. and Li, X., 2014. A ubiquitous low-velocity layer at the base of the mantle transition zone. *Geophys. Res. Lett*., 41, 836–842.

Shen, Y., and Blum, J., 2003. Seismic evidence for accumulated oceanic crust above the 660-km discontinuity beneath southern Africa. *Geophys. Res. Lett.,* 30, 1925, doi: 10.1029/2003GL017991, 18.

Shorttle, O., Mavlennan, J. and Lambart, S., 2014. Quantifying lithological variability in the mantle, *Earth Planet. Sci. Lett.,* 395, 24-40.

Sinogeikin, V.S., Bass, J.D., Kavner, A. and Jeanloz, R., 1997. Elasticity of natural majorite and ringwoodite from the catherwood meteorite. *Geophys. Res. Lett*., 24, doi: 10.1029/97GL03217.

Sinogeikin, S. V., and Bass, J.D., 2002. Elasticity of Majorite and a Majorite-Pyrope solid solution to high pressure: Implications for the Transition Zone. *Geophys. Res. Lett*., 29, doi: 10.1029/2001GL013937, 2002.

Stammler, K., Kind, R., Petersen, N., Korsarev, G., Vinnik, L. and Qiyuan, L., 1992. The upper mantle discontinuities: Correlated or anticorrelated? *Geophys. Res. Lett.,* 15, 1563-1566.

Stixrude, L. and Lithgow-Bertelloni, C., 2011. Thermodynamics of mantle minerals - II. Phase equilibria. *Geophys, J. Int.*, 184, 1180-1213.

Stixrude, L. and Lithgow-Bertelloni, C., 2012. Geophysics of Chemical Heterogeneity in the Mantle. *Annu. Rev. Earth Planet. Sci.*, 40, 569–595.

Tauzin, B., and Ricard, Y., 2014. Seismically deduced thermodynamics phase diagrams for the mantle transition zone. *Earth Planet. Sci. Lett.,* 401, 337-346.

Vinnik, L.P., 1977. Detection of waves converted from P to SV in the mantle. *Phys. Earth Planet. Inter.*, 15, 39–45.

Vinnik, L., Kosarev, G. and Petersen, N., 1996. Mantle transition zone beneath Eurasia. *Geophys. Res. Lett.*, 23, 1485-1488.

Vinnik, L. P., Foulger, G.R. and Du, Z., 2005. Seismic boundaries in the mantle beneath Iceland: a new constraint on temperature. *Geophys. J. Int.,* 160, 533–538.

Vinnik, L., and Farra, V., 2006. S velocity reversal in the mantle transition zone*,* *Geophys. Res. Lett.*, 33, L18316, doi:10.1029/2006GL027120.

Xu, W., Lithgow-Bertelloni, C., Stixrude, L., Ritsema, J. 2008. The effect of bulk composition and temperature on mantle seismic structure, *Earth Planet. Sci. Lett,* 275, 70-79.

Yu, Y.G., Wentzcovitch, R.M., Tsuchiya, T., Umemoto, K. and Weidner, D.J., 2007. First principles investigation of the postspinel transition in Mg2SiO4. *Geophys. Res. Lett.*, 34, L10306, doi:10.1029/2007GL029462.

Zhu, L., and Kanamori, H., 2000. Moho depth variation in southern California from teleseismic receiver functions, *J. Geophys. Res.,* 105(B2), 2969–2980, doi: 10.1029/1999JB900322.

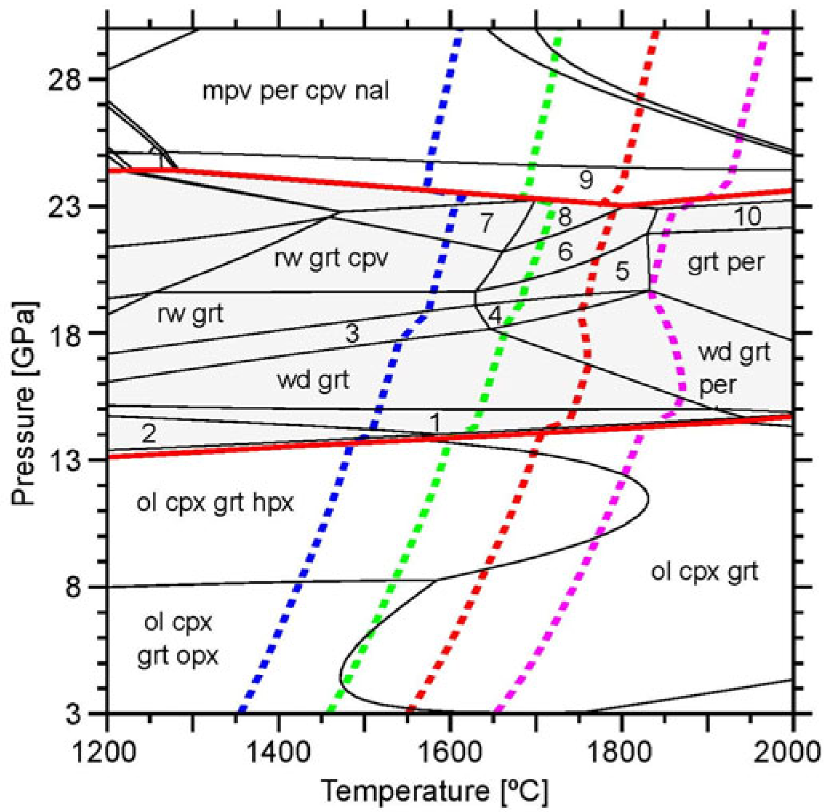

mpv per cpv nal
9
7
8
10
6
5
rw grt cpv
grt per
rw grt
4
3
wd grt
wd grt
per
1
2
ol cpx grt hpx
ol cpx grt
ol cpx
grt opx
28
23
18
13
8
3
1200
1400
1600
1800
2000
Pressure [GPa]
Temperature [ºC]

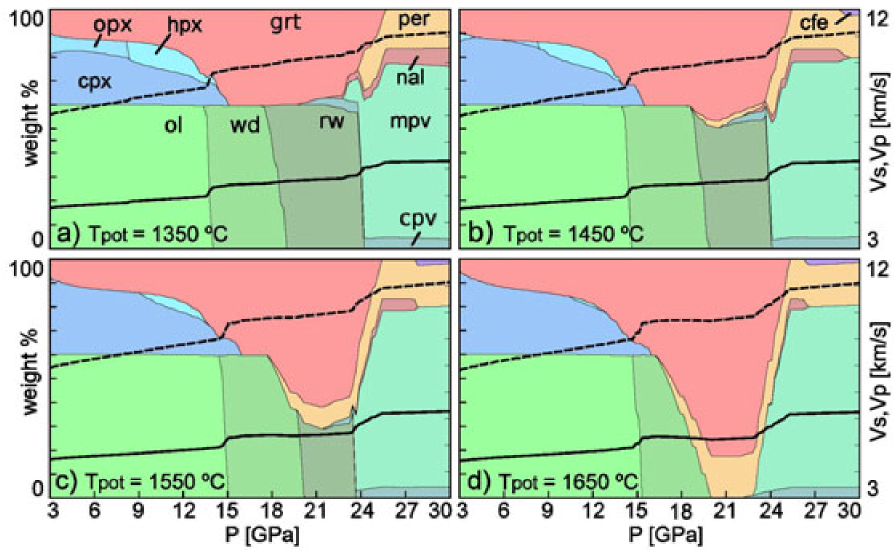
100
0
weight %
opx
hpx
grt
per
cpx
nal
ol
wd
rw
mpv
cpv
a) Tpot = 1350 °C
cfe
12
3
Vs,Vp [km/s]
b) Tpot = 1450 °C
c) Tpot = 1550 °C
d) Tpot = 1650 °C
3 6 9 12 15 18 21 24 27 30
P [GPa]

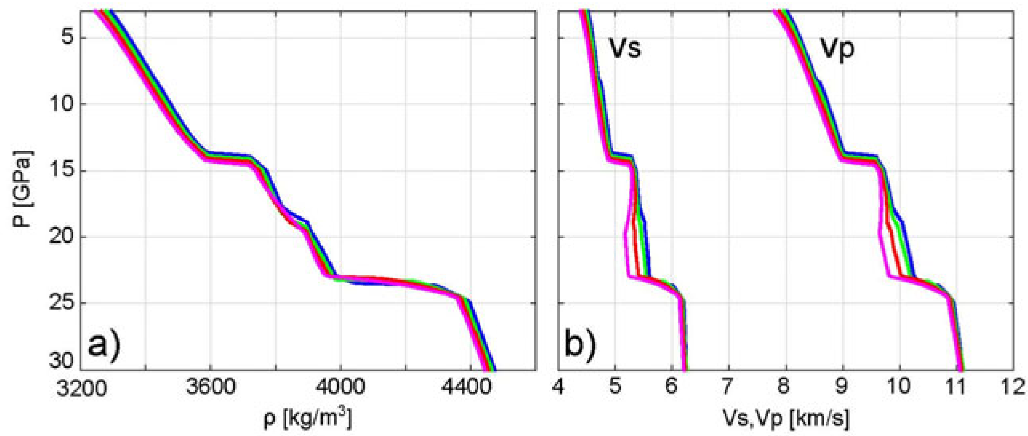
P [GPa]
a)
ρ [kg/m3]
b)
Vs
Vp
Vs,Vp [km/s]

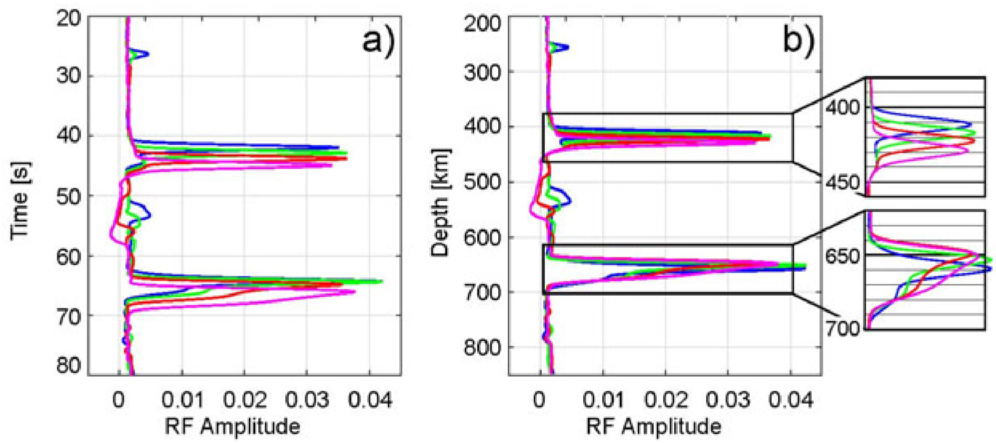
a)
b)
Time [s]
20
30
40
50
60
70
80
Depth [km]
200
300
400
500
600
700
800
0
0.01
0.02
0.03
0.04
RF Amplitude
400
450
650
700

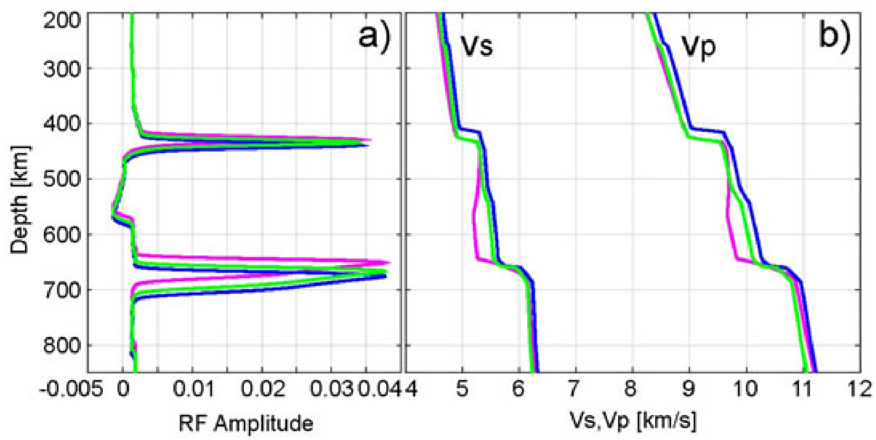
a)
b)
Vs
Vp
Depth [km]
200
300
400
500
600
700
800
-0.005
0
0.01
0.02
0.03
0.04
RF Amplitude
4
5
6
7
8
9
10
11
12
Vs,Vp [km/s]